

Large-Eddy Simulations of Subsonic Impinging Jets

L. Nguyen, V. Golubev, and R. Mankbadi

Abstract—We consider here the subsonic impinging jet representing the flow field of a vertical take-off aircraft or the initial stage of rocket launching. Implicit Large-Eddy Simulation (ILES) is used to calculate the time-dependent flow field and the radiate sound pressure associated with jet impinging. With proper boundary treatments and high-order numerical scheme, the near field sound pressure is successfully obtained. Results are presented for both a rectangular as well a circular jet.

Keywords—Aeroacoustics, Large-Eddy Simulations, Jets, Fluid Dynamics.

I. INTRODUCTION

OUR focus herein is on the acoustic field associated with a subsonic jet impinging on perpendicular flat plate. The problem is relevant to the early take-off stages of Vertical Aircrafts, and for thrust reversers. Strong acoustic loads generated by the impinging jets are an unavoidable design challenge. Acoustic noise at high levels can affect structural and mechanical components on the vehicle itself and may also harm sensitive payloads. These are some of the reasons why developing predictive methods to characterize and accurately describe noise levels generated within the exhaust plumes are desirable. In a later stage, we will consider the supersonic case (as in Brown & Frendi1), but our efforts here is on subsonic jets in an attempt to identify the mechanisms involved without the presence of shock waves.

In a classical paper, Ho and Nosseir2 performed testing with turbulent impinging jets with high subsonic exit Mach numbers with emphasis on identifying the feedback mechanisms involved. Their test data showed that for high subsonic speeds ($M > 0.7$) and nozzle exit to plate separation distances of less than 7.5 exit diameters, the measured pressure signal on the plate has a sine shape indicating resonance. Nosseir and Ho3 examined the noise radiated by the jets and their far field pressure measurements showed that there are staging in the data. Their cross correlations of the pressure data showed that the primary source of noise was the plate for a jet in resonance. Tam and Ahuja4 suggested that the feedback loop for the impingement tones is not external to the jet as put forth by Nosseir and Ho3 . Tam and Ahuja4 proposed that the waves travelling upstream from the plate to the nozzle exit are neutral waves with characteristics that resemble that of Kelvin Helmholtz instability waves. These waves propagate within the jet and close the feedback loop, which produces the characteristic impingement tones.

L. Nguyen, V. Golubev, and R. Mankbadi are with the Embry-Riddle Aeronautical University, Daytona Beach, FL 32114.

II. FLUID DYNAMIC MODEL

The governing equations for the current numerical simulations are the compressible Navier-Stokes equations represented in strong, conservative, time-dependent form in the generalized curvilinear computational coordinates (ξ, η, ζ, τ) transformed from the physical coordinates (x, y, z, t) :

$$\frac{\partial}{\partial \tau} \left(\frac{\vec{Q}}{J} \right) + \frac{\partial \vec{F}_i}{\partial \xi} + \frac{\partial \vec{G}_i}{\partial \eta} + \frac{\partial \vec{H}_i}{\partial \zeta} + \frac{1}{\text{Re}} \left[\frac{\partial \vec{F}_v}{\partial \xi} + \frac{\partial \vec{G}_v}{\partial \eta} + \frac{\partial \vec{H}_v}{\partial \zeta} \right] = \vec{S} \quad (1)$$

The solution vector $\vec{Q} = (\rho, \rho u, \rho v, \rho w, \rho e)$ is defined in terms of the flow density ρ , Cartesian flow velocity components (u, v, w) , and flow specific energy,

$$e = \frac{T}{\gamma(\gamma - 1)M_\infty^2} + \frac{1}{2}(u^2 + v^2 + w^2)$$

with assumed perfect gas relationship connecting the flow pressure p , temperature T , and the freestream Mach number M_∞ (γ is the specific heat ratio). The other variables in (1) include the inviscid flux vectors defined by

$$\vec{F}_i = \begin{bmatrix} \rho \hat{u} \\ \rho u \hat{u} + \hat{\xi}_x p \\ \rho v \hat{u} + \hat{\xi}_y p \\ \rho w \hat{u} + \hat{\xi}_z p \\ (\rho e + p) \hat{u} - \hat{\xi}_i p \end{bmatrix}$$

$$\vec{G}_i = \begin{bmatrix} \rho \hat{v} \\ \rho u \hat{v} + \hat{\eta}_x p \\ \rho v \hat{v} + \hat{\eta}_y p \\ \rho w \hat{v} + \hat{\eta}_z p \\ (\rho e + p) \hat{v} - \hat{\eta}_i p \end{bmatrix}$$

$$\vec{H}_i = \begin{bmatrix} \rho \hat{w} \\ \rho u \hat{w} + \hat{\zeta}_x p \\ \rho v \hat{w} + \hat{\zeta}_y p \\ \rho w \hat{w} + \hat{\zeta}_z p \\ (\rho e + p) \hat{w} - \hat{\zeta}_t p \end{bmatrix} \quad (2)$$

the transformation Jacobian is $J = \partial(\xi, \eta, \zeta, \tau) / \partial(x, y, z, t)$, the metric quantities defined, e.g., as $\hat{\xi}_x = (J^{-1}) \partial \xi / \partial x$, etc., and the transformed flow velocity components are,

$$\begin{aligned} \hat{u} &= \hat{\xi}_t + \hat{\xi}_x u + \hat{\xi}_y v + \hat{\xi}_z w \\ \hat{v} &= \hat{\eta}_t + \hat{\eta}_x u + \hat{\eta}_y v + \hat{\eta}_z w \\ \hat{w} &= \hat{\zeta}_t + \hat{\zeta}_x u + \hat{\zeta}_y v + \hat{\zeta}_z w \end{aligned} \quad (3)$$

The viscous flux vectors, \vec{F}_v , \vec{G}_v and \vec{H}_v , are defined in Ref. [5]. All flow variables are normalized by their respective reference freestream values except for pressure, which is nondimensionalized by $\rho_\infty u_\infty^2$.

Note that the governing equations are represented in the original unfiltered form used are unchanged in laminar, transitional, or fully turbulent regions of the flow. Refs [6-7] provide details on the Implicit LES procedure employed in the numerical code in which a high-order low-pass filter operator is applied to the dependent variables during the solution process, in contrast to the standard LES addition of sub-grid stress (SGS) and heat flux terms. The resulting filter selectively damps the evolving poorly resolved high-frequency content of the solution.

The numerical simulations are conducted using a high-order Navier-Stokes solver *FDL3DI*, which has been extensively validated for a variety of complex unsteady flows⁸. The code employs a finite-difference approach to discretize the governing equations, with all the spatial derivatives obtained using the high-order compact-differencing schemes from Ref. [9]. For the current paper, a sixth-order scheme is used. At boundary points, higher-order one-sided formulas are utilized which retain the tridiagonal form of the scheme. In order to ensure that the Geometric Conservation Law (GCL) is satisfied, the time metric terms are evaluated using the procedures described in detail in Ref. [7]. Finally, the time marching is accomplished by incorporating a second-order iterative; implicit approximately factored procedure as described in Refs [6-8].

III. NUMERICAL IMPLEMENTATION

Results shown below are obtained for two different jet configurations: a planar jet exit impinging upon a flat plate normal to the jet stream and for the flow of a round jet

impinging on a perpendicular flat plate. Initially, for the planar jet, 2D numerical grids were investigated to determine the optimal configuration needed to achieve adequate accuracy of the numerical solutions with minimum computational costs. Both planar 2D and 3D computational mesh features an H-grid topology with 390×498 points in the streamwise and normal direction, respectively. Along the span, the 2D mesh requires 3 points to accommodate the high-order scheme, while the 3D mesh has 51 points distributed among a span of 0.3R.

Fig. 1 illustrates the mesh configuration used herein. Fig. 1a shows the location of the flat plate, represented by the green line, located 22.75R away from the inlet, where R is the radius of the jet set as a non-dimensionalized value of 1. The boundary condition specified along the surface of the flat plate is a no-slip, adiabatic wall with 4th order extrapolation. At 50R away from the inlet in the normal direction, a freestream condition with 1st-order extrapolation is applied to the farfield (purple) with the grid stretching towards the boundary to ensure effective elimination of spurious reflections achieved in conjunction with the low-pass spatial filtering⁸. Along the jet centerline (blue), a symmetry condition with 2nd-order extrapolation is imposed. Fig. 1b shows the jet exit (inlet of the mesh) in which a top-hat profile is prescribed with a Mach (M) and Reynolds (Re) number of 0.5 and 1,270,000 are chosen, respectively. Adjacent to the jet exit, similar to farfield, a freestream condition is applied at X=0 and Y= (1, 50) (purple).

TABLE I
 DETAILS OF COMPUTATIONAL MESH DIMENSION

Mesh	Dimension
2D	$390 \times 498 \times 3$
3D	$390 \times 498 \times 51$

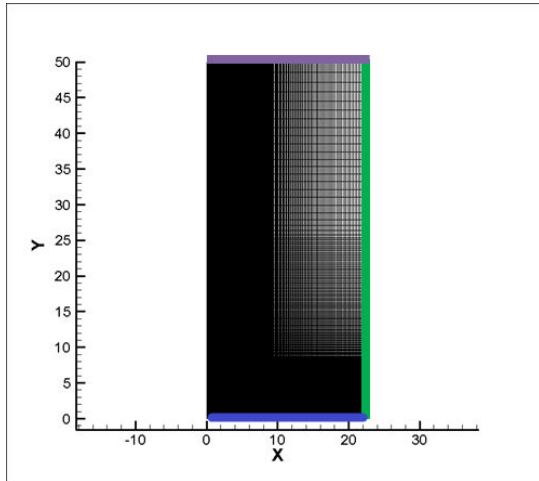
For the second configuration, a full 3D round jet computational domain is created as illustrated in Fig. 2. The rectangular mesh features $71 \times 255 \times 255$ points in the streamwise, normal, and span, respectively with points clustered at R=1 measured from the center of the domain.

Fig. 3 shows the exit of the jet with a selected value of R=1 similar to the planar jet configuration. Fig. 3 (a) reveals areas of high resolution immediately around the exit of the jet, which is crucial for capturing the interactions of the jet stream and freestream conditions. To examine the effects of an impinging jet, 8R away downstream of the jet exit is the end of the computational domain, which is where the flat plate prescribed as a solid wall is located (Fig. 3b, red). The extent of domain allows for an $x/d=4$. The boundary conditions specified along the four sides (purple) of the computational domain is the same used for farfields in the previous planar jet; freestream condition with 1st-order extrapolation. The jet exit, Fig. 3b, is also prescribed with a similar condition as the previous grid, M=0.5 as well as M=0.9 and Re=1,270,000. Adjacent to the jet exit, a freestream condition with 1st-order extrapolation is prescribed shown in Fig. 3 (b).

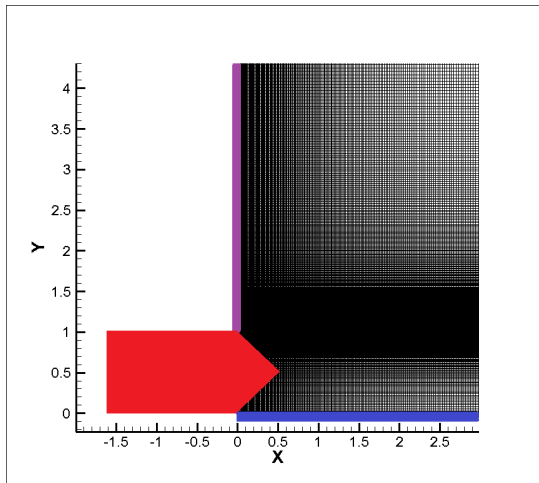
$$u_z(r) = u_j \frac{r_o - r}{\delta} \left[2 - 2 \left(\frac{r_o - r}{\delta} \right)^2 + \left(\frac{r_o - r}{\delta} \right)^3 \right], \quad \text{if } r \geq r_o - \delta,$$

$$u_z(r) = u_j, \quad \text{if } r < r_o - \delta,$$

The computational domain features near-uniform spacing in the x-direction of 0.1 non-dimensional length. Along the jet radius of R=1, as shown in Fig. 3 (a), the spacing is reduced to 0.017 to achieve better accuracy.

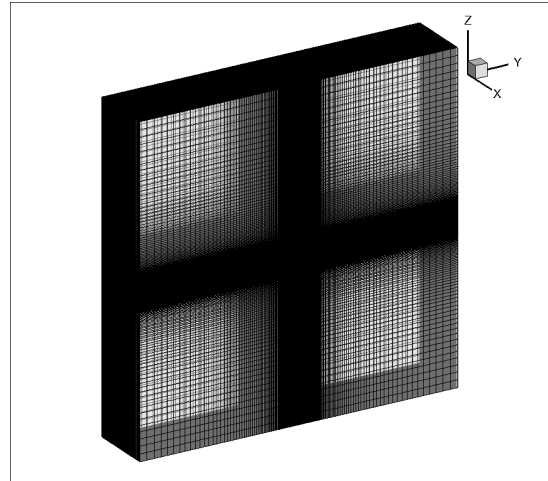


(a)

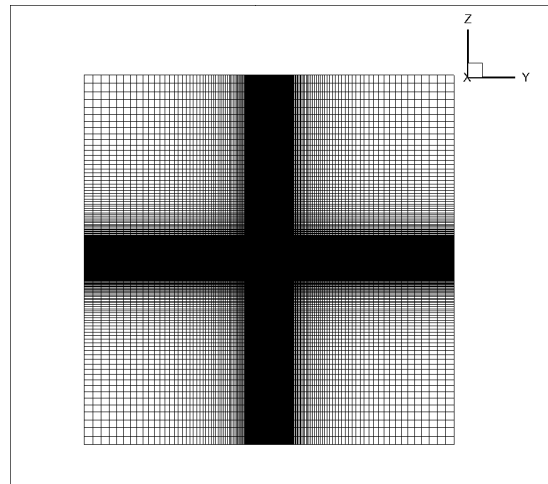


(b)

Fig. 1 Details of baseline planar 2D and 3D computational mesh
 (a) Full side view and (b) zoomed

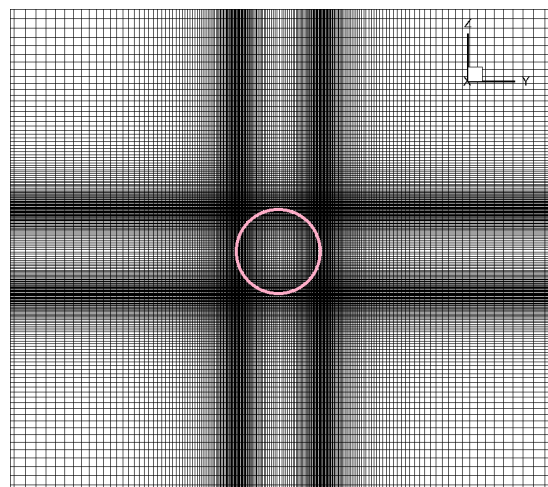


(a)



(b)

Fig. 2 Details of 3D round jet computational mesh (a) ISO view and (b) front view



(a)

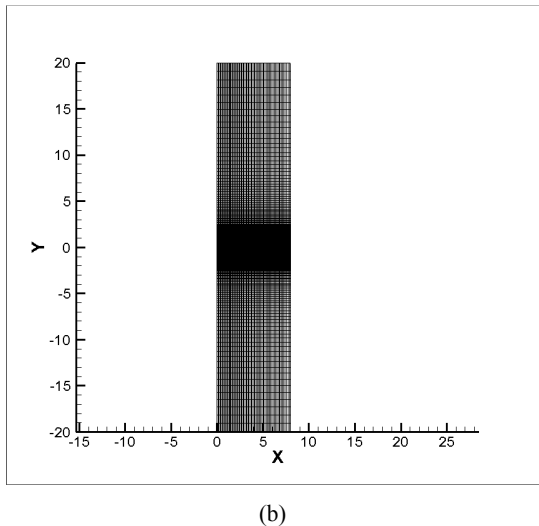


Fig. 3 Details of jet exit (a) Front and (b) side view illustrating location (pink)

IV. RESULTS

A. 2D Subsonic Jet Impinging on Perpendicular Flat Plate

Quasi-steady solutions are obtained by advancing for 20 characteristic cycles from initialization to remove any spurious transient data and guarantee a time-asymptotic nearly-periodic state. The pressure field shown below in fig. 4 reveals the acoustic propagation as a result of the jet exit mixing with the freestream conditions. The full view provides details of the Jetstream affecting the farfield, while the zoom view reveals the results of the nearfield. The nearfield results in fig. 4 shows the jet stream impinging against the flat plate and forming an area of recirculation revealing itself as large blue patterns. This is future illustrated in the turbulent kinetic energy (TKE) in Fig. 5.

B. 3D Subsonic Jet Impinging on Perpendicular Flat Plate

Similar to 2D results, 3D Quasi-steady solutions are obtained by advancing for 20 characteristic cycles from initialization. The pressure field shown below in fig. 6 reveals more distinct acoustic pattern than the previous 2D results with smaller areas of recirculation. This is due to turbulent redistribution in the spanwise direction, which allows the large vortical scales to break down into smaller ones. The 3D results show a similar trend to the 2D computations with slight differences in the mixing layer and recirculation area. Figure 7 shows the 3D TKE, which is very similar to 2D results, however the overall structure is more coherent than 2D.

C. Subsonic Round Jet

Similar to the rectangular jet quasi-steady solutions are obtained by advancing for 20 characteristic cycles from initialization. The results for $M=0.5$ are shown in figures 8-11 while that of $M=0.8$ are shown in Fig. 12-15. In both cases, the pressure field is shown, turbulence kinetic energy, the helical structure, and the spectra. The acoustic near field is evident.

V. CONCLUSIONS

We consider here the subsonic impinging jet representing the flow field of a vertical take-off aircraft or the initial stage of rocket launching. Implicit Large-Eddy Simulation (ILES) is used to calculate the time-dependent flow field and the radiate sound pressure associated with jet impinging. With proper boundary treatments and high-order numerical scheme, the near field sound pressure is successfully obtained. Results are presented for both a rectangular as well a circular jet.

Results indicate the initial region of the jet is characterized by axisymmetrical and helical vortical structures. The strong impinging of the jet on the flat plate feeds back into the structure in the initial region of the jet. Despite the strong reflections on the ground, the acoustic near field of the jet seems to be generated by the unsteady structure in the initial region of the jet.

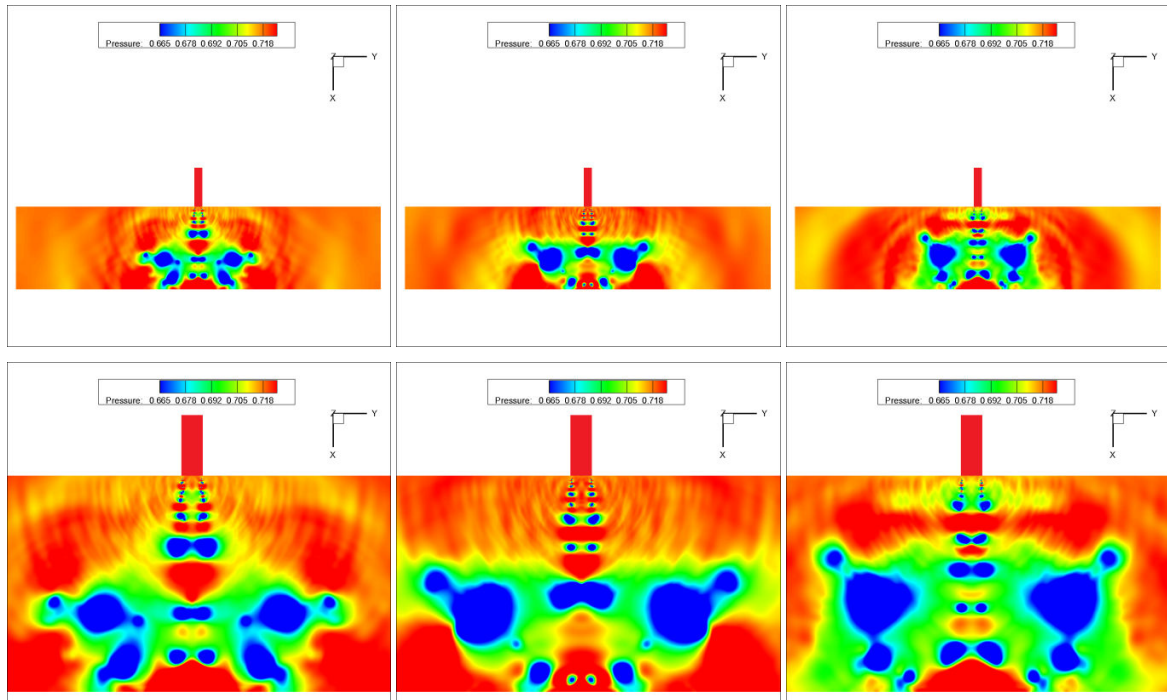


Fig. 4 2D Pressure contours (top) Full view (bottom) zoomed view. $T=34$, $T=36$, and $T=38$, left to right

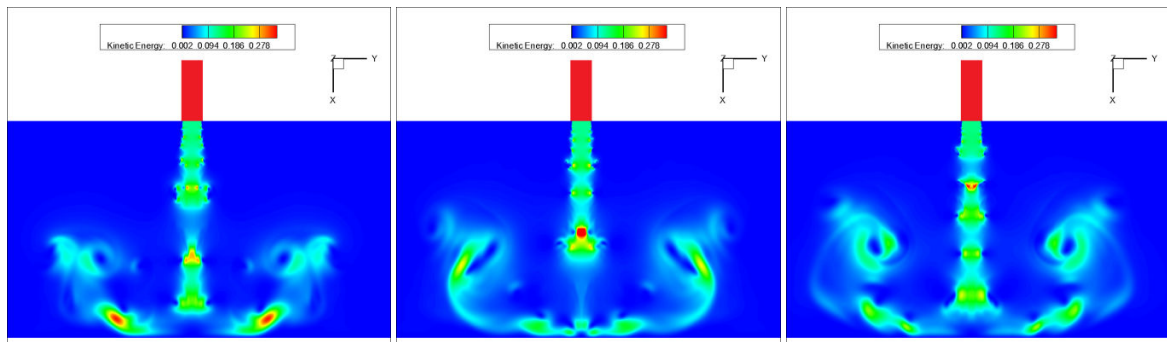


Fig. 5 2D Turbulent Kinetic Energy contours. $T=34$, $T=36$, and $T=38$, left to right

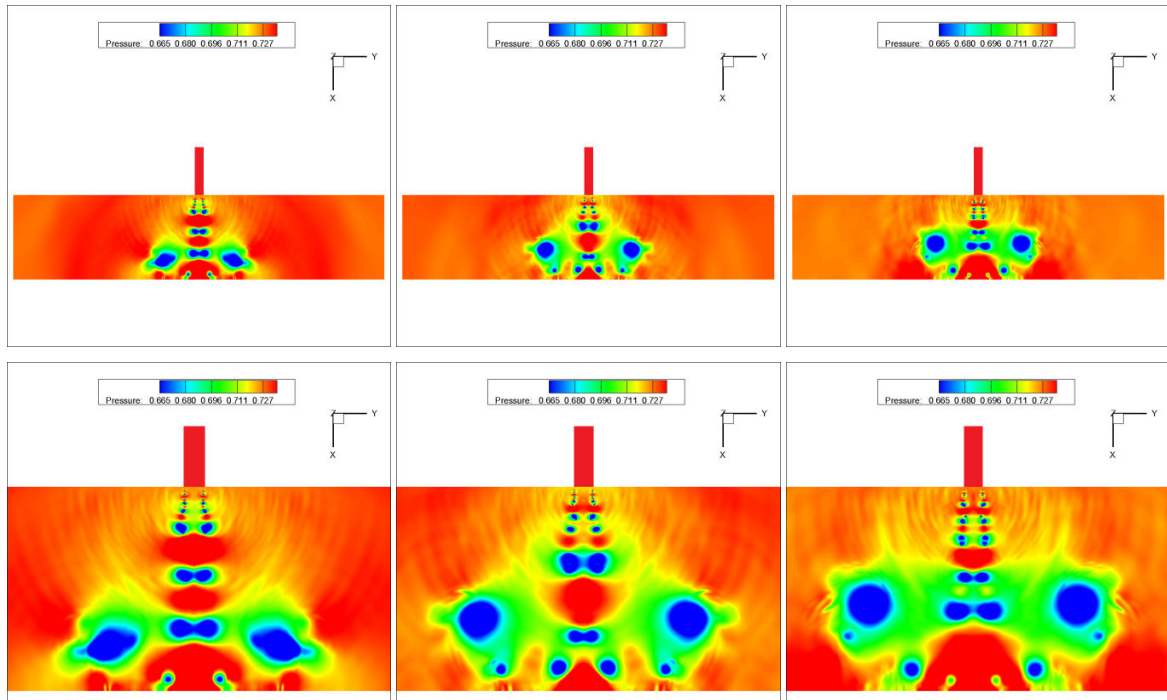


Fig. 6 3D Pressure contours (top) Full view (bottom) zoomed view. $T=34$, $T=36$, and $T=38$, left to right

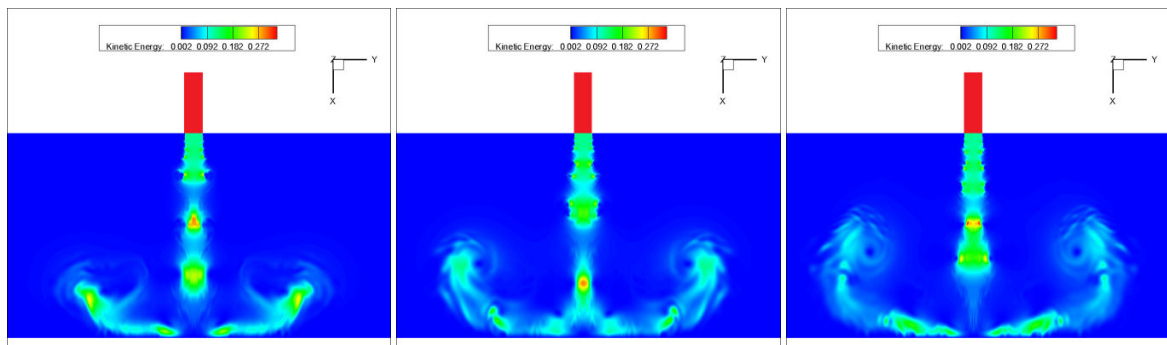


Fig. 7 3D Turbulent Kinetic Energy contours. $T=34$, $T=36$, and $T=38$, left to right

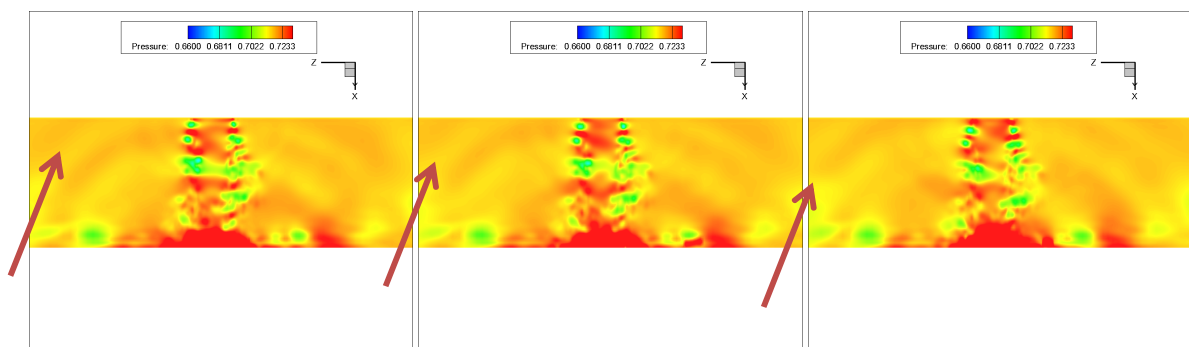


Fig. 8 C. Subsonic Round jet impinging on perpendicular flat plate ($M=0.5$). Instantaneous pressure contours (mid-slice). $T=30.1$, $T=30.2$, and $T=30.3$, left to right

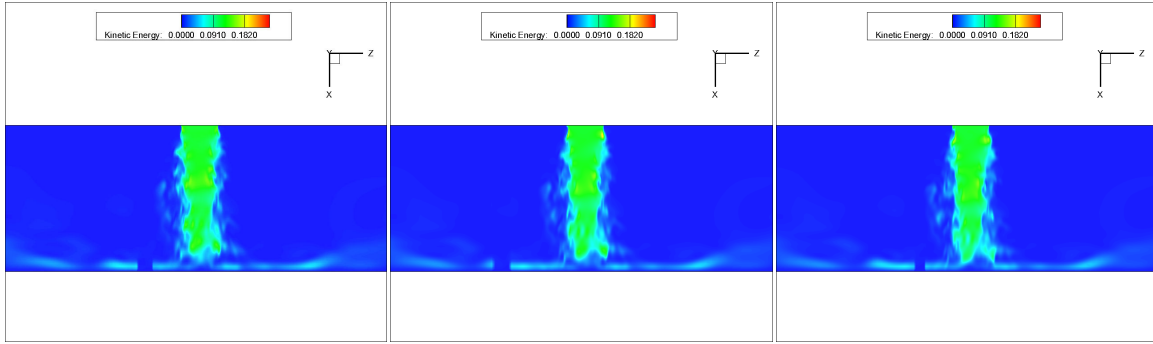


Fig. 9 Instantaneous turbulence kinetic energy (mid-slice) $T=30.1$, $T=30.2$, and $T=30.3$, left to right

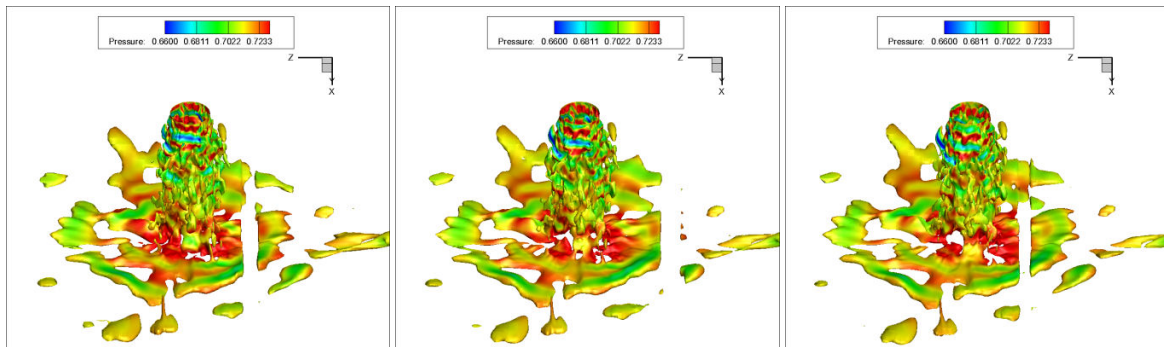


Fig. 10 Instantaneous Mach=0.2 isosurfaces colored by pressure. $T=30.1$, $T=30.2$, and $T=30.3$, left to right.

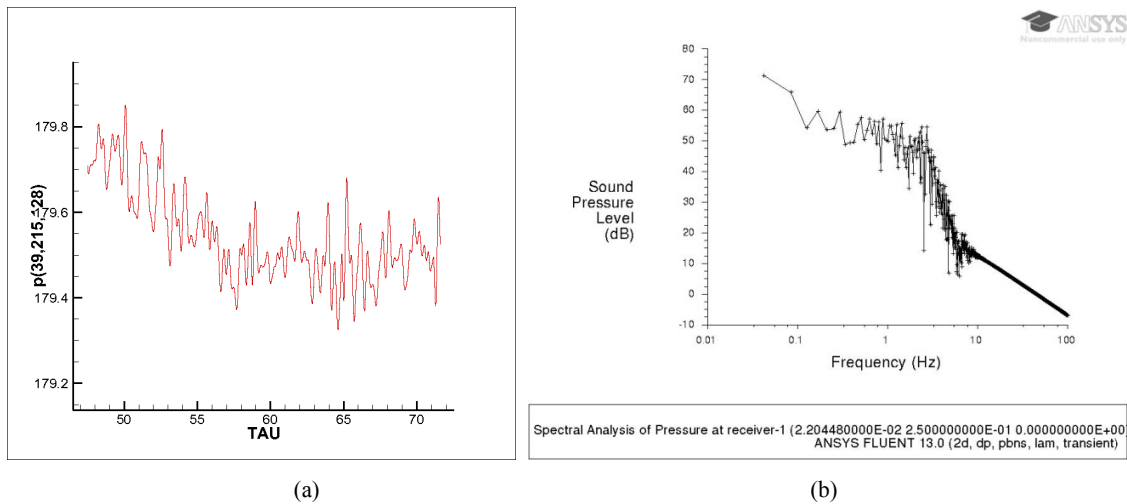


Fig. 11 (a) Nearfield pressure time history and (b) Sound pressure level at $M=0.5$ Subsonic Round jet impinging on perpendicular flat plate ($M=0.8$)

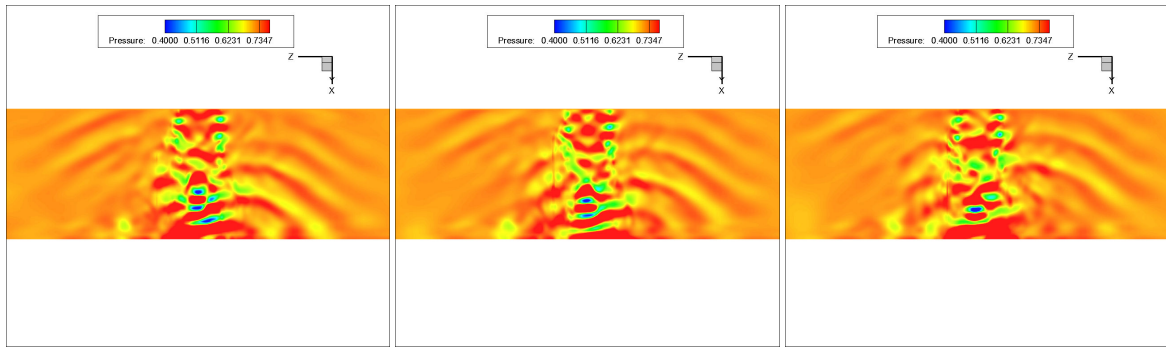


Fig. 12 D Subsonic Round jet impinging on perpendicular flat plate ($M=0.8$) Instantaneous pressure contours (mid-slice). $T=30.1$, $T=30.2$, and $T=30.3$, left to right

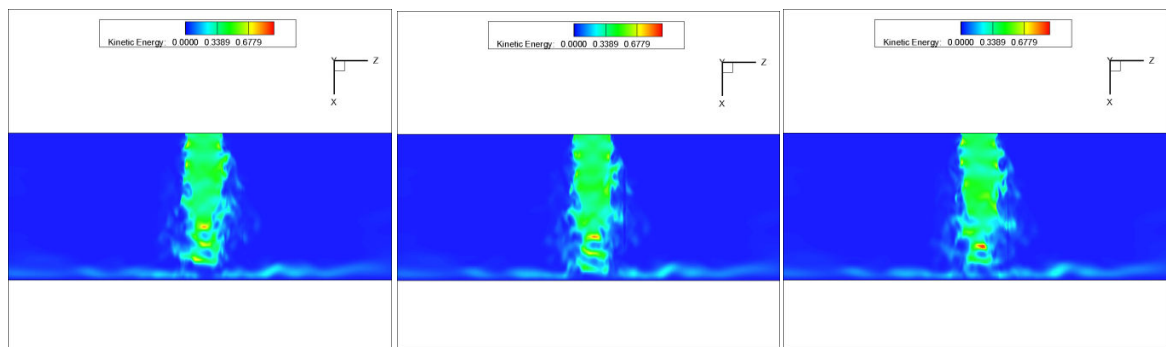


Fig. 13 Instantaneous turbulence kinetic energy (mid-slice) $T=30.1$, $T=30.2$, and $T=30.3$, left to right

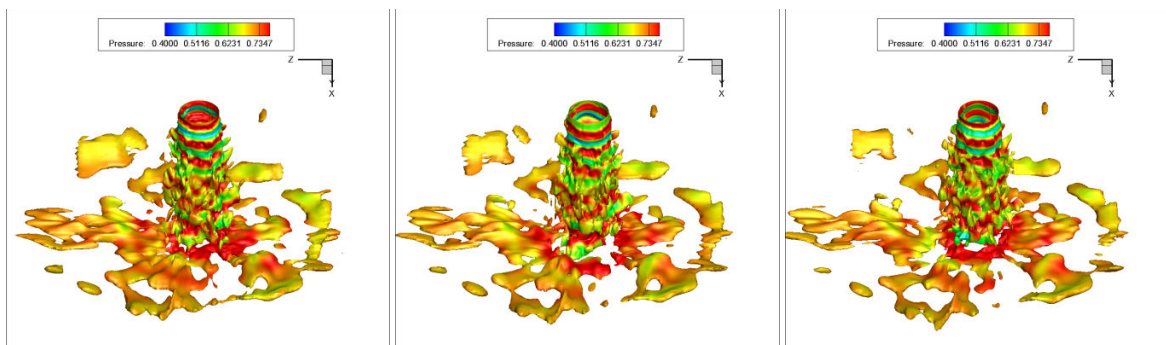


Fig. 14 Instantaneous Mach=0.5 isosurfaces colored by pressure $T=30.1$, $T=30.2$, and $T=30.3$, left to right

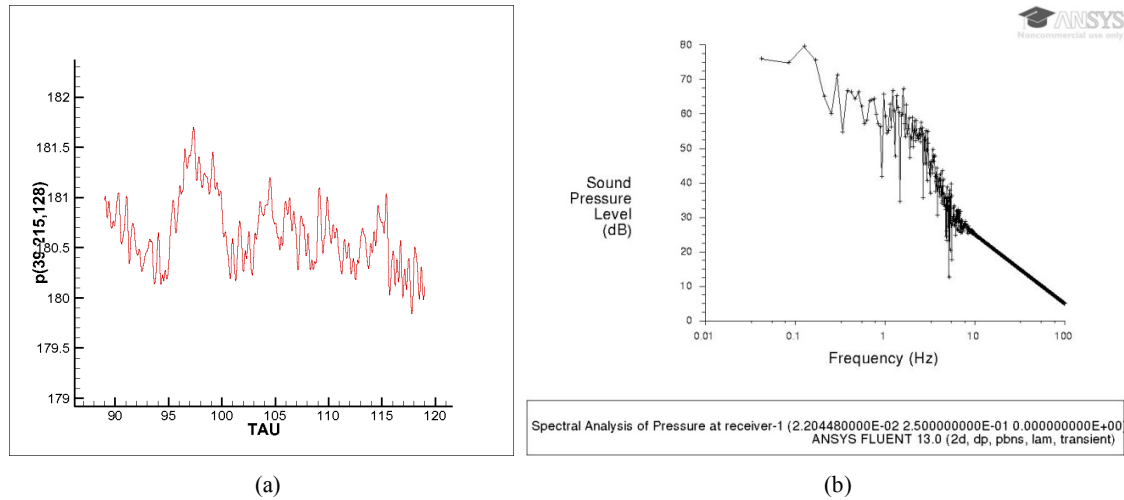


Fig. 15 (a) Nearfield pressure time history and (b) Sound pressure level at $M=0.9$

ACKNOWLEDGMENTS

The support of the Florida Center for Advanced Aero propulsion is greatly appreciated.

REFERENCES

- [1] Brown, M, & Frendi, A., 2012, "Supersonic Jet Impingement on A Flat Plate," AIAA. 2012-2201, 18th AIAA/CEAS Aeroacoustics Conference, June 2012, Colorado Springs, Co.
- [2] Ho, C. and Nosseir, N. S., "Dynamics of an impinging jet, Part 1, The feedback Phenomenon", Journal of Fluid Mechanics, Vol. 105, pp. 119-142, 1981.
- [3] Nosseir, N.S. and Ho, C., "Dynamics of an impinging jet, Part 2, the noise generation", Journal of Fluid Mechanics, Vol. 116, pp. 379-391, 1982.
- [4] Tam, C.K.W. and Ahuja, K.K., "Theoretical model of discrete tone generation by impinging jets", Journal of Fluid Mechanics, Vol. 214, pp. 67-87, 1990.
- [5] Anderson, D.A., Tannehill, J.C. and Pletcher, R.H., "Computational Fluid Mechanics and Heat Transfer," McGraw-Hill Book Company, 1984.
- [6] Visbal, M.R. and Rizzetta, D.P., (2002) "Large-Eddy Simulation on Curvilinear Grids Using Compact Differencing and Filtering Schemes," Journal of Fluids Engineering, Vol. 124, pp.836-847.
- [7] Visbal, M.R., Morgan, P.E. and Rizzetta, D.P., (2003) "An Implicit LES Approach Based on High-Order Compact Differencing and Filtering Schemes," AIAA Paper 2003-4098.
- [8] Visbal, M.R. and Gaitonde, D.V., (2002), "On the Use of High-Order Finite-Difference Schemes on Curvilinear and Deforming Meshes," Journal of Computational Physics, Vol. 181, pp.155-185, 2002.
- [9] Lele, S.K., (1992) "Compact Finite Difference Schemes with Spectral-like Resolution," Journal of Computational Physics, 103, pp16-42.